Tribology International 210 (2025) 110820

Contents lists available at ScienceDirect

Tribology International

journal homepage: www.elsevier.com/locate/triboint

The evolution of contact conditions during fretting wear tests with cylinder-on-flat and crossed-cylinder specimen configurations

A.J. Gichuki [*], P.H. Shipway, J.P. Rouse, C.J. Bennett, D. Koti, E. Coll

Mechanical and Aerospace Systems Research Group (MAS), the University of Nottingham, NG7 2TU, UK

ARTICLE INFO

Keywords:
Steel
Wear characterisation
Non-conforming contacts
Size-dependent specific wear rate

ABSTRACT

This study examines the dependence of fretting wear of a high strength steel using four non-conforming specimen configurations: cylinder-on-flat and crossed-cylinders, with both 6 mm and 160 mm radii cylinders. In each configuration, the wear of the two bodies is well described by their geometrical volume of intersection. A predictive model indicated significant differences in the evolution of the size and depth of the wear scar and contact pressure in the four cases considered; despite this, the size-dependent specific wear rates evaluated were similar to each other (between 24.5 and 43.5 $\text{mm}^4\,\text{MJ}^{-1}$). Furthermore, oxide debris formation was shown to depend on contact size rather than pressure; smaller contact sizes favoured protective debris-bed formation limiting subsurface plasticity in the specimens.

1. Introduction

Fretting wear is a common issue in applications with small relative displacement between machine-component interfaces which can result in a loss of critical tolerances and efficiency. Fretting wear differs from wear in sliding in that the contact remains largely closed during the process, and therefore, in steady state, the process of wear involves both the formation of debris and then its subsequent transport across the contact interface so that it can be removed from the contact, thus allowing wear to proceed. In some cases, the wear debris may be formed by an interaction or reaction of the material at the wearing surfaces with species from the environment, and in these cases, the relevant species from the environment must also be transported across the contact interface to facilitate this. This is generally the case in the fretting wear of non-noble metals (such as steels and titanium alloys), where the debris is typically in the form of an oxide which, therefore, requires oxygen transport to the wearing surfaces through the contact. As such, within the overall process of fretting wear, there are number of sub-processes which rely on transport of species across the contact interface [1]. Accordingly, it has long been argued that the rate of fretting wear will depend upon the physical dimensions of the wearing contact [2], with recent work addressing this issue and developing models of this dependence [1,3]; further background relating to the role that the contact size has in fretting wear can be found in these two publications. A key corollary to the existence of a size effect in fretting is that if the contact size changes as wear takes place (either in laboratory testing or for in-service situations), then the rate of wear will change during the process even if all other parameters remain the same. This concept is clearly inconsistent with any predictive wear formulation which suggests that the wear volume is proportional to some measure of the exposure to wear. As such, we argue that the following two formulations which are widely used in the analysis of fretting wear are (in general) inconsistent with the concept of a size effect in fretting wear:

$$V = k_{energy}E \tag{1}$$

and

$$V = k_{Archard}\,P\,4\delta\,N \tag{2}$$

where V is the wear volume, E is the frictional energy dissipated over the course of a test, P is the applied load, δ is the slip amplitude, N is the number of cycles in the test and k is the relevant specific wear rate (sometimes termed the wear coefficient).

We assert that such formulations for V should never be employed for non-conforming contacts; moreover, if they are used to describe the behaviour in conforming contacts, it must be recognised that the specific wear rates so derived (either k_{energy} or $k_{Archard}$) are relevant only to the specific contact configuration employed. It is obvious that this has implications for laboratory fretting testing, both in interpretation of existing data in the literature, and in terms of design of future experimental programmes. Laboratory fretting tests are commonly employed

---

[*] Corresponding author.
E-mail address: Allan.Gichuki@nottingham.ac.uk (A.J. Gichuki).

https://doi.org/10.1016/j.triboint.2025.110820
Received 31 October 2024; Received in revised form 7 May 2025; Accepted 19 May 2025

Nomenclature

BSE	Backscattered electron
CoF	Cylinder-on-flat
C×C	Crossed-cylinder (cylinder-on-cylinder)
EDX	Energy-dispersive X-ray
FoF	Flat-on-flat
R6	Cylinder specimen with a radius 6 mm
R160	Cylinder specimen with a radius 160 mm
RDP	Rate-determining process
SEM	Scanning electron microscopy
SoF	Sphere-on-flat

in work seeking to (i) understand the effect of various test parameters on the wear process, (ii) compare the wear behaviour of different materials, and (iii) predict the rate of wear in a service environment. Commonly employed contact configurations are flat-on-flat (FoF), cylinder-on-flat (CoF), sphere-on-flat (SoF) and crossed-cylinders (C×C). The conforming FoF configuration has the key advantage over the other configurations in that the contact size does not change as the test proceeds, but as Baydoun et al. [4] recently noted "*few are the researches that examined fretting wear using flat-on-flat geometry due to its high sensitivity to alignment issues*".

A brief survey of the literature which reports laboratory wear testing indicates that the most commonly employed contact configurations are in the group of non-conforming configurations. In such tests, as the test proceeds, the contact size increases and the contact pressure decreases and thus is it difficult to deconvolute these two effects [5]; moreover, it is recognised that such changes in size and contact pressure may be responsible not only for differences in rates of wear but also for differences in modes of wear, and specifically whether the contact forms a U-shaped wear scar or a W-shaped wear scar [5]. Such deconvolution of the roles of contact size and contact pressure can only be properly achieved in tests with conforming contacts; in this regard, two recent papers by Baydoun et al. conducted with conforming contact configurations have clearly demonstrated the following: (i) a contact size effect exists in tests conducted with a constant contact pressure of 100 MPa [3]; (ii) wear rates are independent of contact pressure up to 125 MPa but dependent upon pressure at higher values [4].

Equations have recently been derived [6] which describe the development of wear volume in fretting tests between bodies with commonly employed contact configurations (both conforming and non-conforming), with these equations being based only upon the hypothesis that when transport of species (either debris or oxygen) across the contact is the rate-determining process (RDP) [1,7], the instantaneous wear rate $\left(\frac{dV}{dE}\right)$ is inversely proportional to a critical dimension of the contact [8], as follows:

$$\frac{dV}{dE} = \frac{k_{sd}}{x} \tag{3}$$

where k_{sd} is the size-dependent specific wear rate and x is the relevant critical dimension of the wear scar. Moreover, recent reanalysis of published data has demonstrated the broad applicability of this approach for the various contact configurations [6].

For the CoF contact geometry, the equation which describes the development of wear volume is as follows [6]:

$$0.8585\ V^{4/3}\left(\frac{R}{L}\right)^{1/3} = k_{sd}E \tag{4}$$

where R is the radius of the cylinder in the contact and L is the line contact length between the flat and the cylinder, Fig. 2**a**.

For the SoF or C×C contact geometries, the equation which describes the development of wear volume is as follows [6]:

$$0.8498\ V^{5/4}R^{1/4} = k_{sd}E \tag{5}$$

where R is the radius of either the sphere or the two cylindrical specimens which make up the contact, Fig. 2**b**.

The derivation of these equations is based upon the hypothesis that the combined wear volume of the two bodies can be described by the geometrical volume of intersection of one body with the other, this being a prismatic minor segment of a circle for the CoF contact configuration (Fig. 1**a**) and a spherical cap for the SoF and C×C contact configurations (Fig. 1**b**) [9]. The validity of this hypothesis was demonstrated for the CoF contact configuration by comparisons of measured and predicted wear volumes as a function of worn contact width [8]; however, the validity of the hypothesis has not yet been demonstrated for the SoF / C×C contact configuration. This demonstration is the main focus of the presented work.

In previous work, the concept of a size-dependent specific wear rate has been effectively used to rationalise observed differences in development of wear volume with energy dissipated for contacts of a specific configuration (either CoF or SoF) as a function of the radii of the non-plane body within the contacts [9]. However, it has not yet been used to compare data and size-dependent specific wear rates generated from tests conducted with different contact configurations; this is a critical step in proving the general applicability of the method.

In a fretting contact between two metallic bodies, the metals are initially in contact but as fretting commences, debris is generated. Under some conditions, a debris bed (the third body) forms which separates the metallic bodies (the first bodies) from each other, and the nature of this debris bed will influence the process of development of wear and damage. Thick, coherent debris beds will effectively separate the first bodies from each other, whereas with thinner, less coherent or non-existent beds, interaction between the first bodies will be significant. It has been shown that with thick, coherent debris beds, sub-surface plastic damage in the first bodies is minimal, whereas when the debris beds are less coherent or non-existent, then significant sub-surface plasticity in the first bodies is observed [10]. Moreover, it has been shown that the changes in test conditions can result in a change in the type of sub-surface damage and that this itself provides evidence with regard to the mechanism of formation of the debris bed or not [10]. In work examining the role of contact size in fretting conducted in the CoF contact configuration, it was seen that the tendency for gross material transfer between the first bodies increased as the cylinder radius increased (i.e. with increasing contact size but reduced contact pressure) [8]. No cross-sectional microscopy of the subsurface damage was presented in that work, and thus the nature of the damage could only be inferred.

Whilst the broad applicability of this approach has been demonstrated, it has not yet been used to compare size-dependent specific wear rates generated from tests conducted with different contact configurations and it is argued that this is a critical step in further cementing the general applicability of the method. In this work, for the first time, the same material will be fretted under the same conditions in both the CoF and C×C contact configurations with two very different radii of the cylinders used being employed (both 6 mm and 160 mm). The effectiveness of the size-dependent specific wear rate in describing data from such tests will be examined. Alongside, the nature of the sub-surface damage in the worn contacts will be examined as a means of understanding the dependence of the debris layer characteristics on the characteristics of the contact.

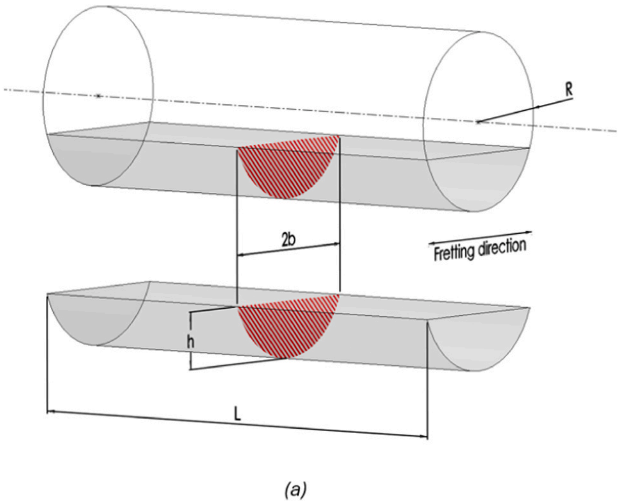

Fig. 1. Proposed combined wear scar geometries for: (a) a cylinder-on-flat configuration; and (b) a sphere-on-flat/crossed-cylinder configuration [9].

2. Methodology

2.1. *Materials and contact configurations*

Specimens used in this study are produced from a high-strength alloy steel, BS S132, with a chemical composition and mechanical properties in Table 1 and Table 2, respectively. The flat and cylindrical specimens were ground on a linear and cylindrical grinder, respectively, for a surface finish of 0.1–0.3 μm (Ra) for the flat specimens and 0.4–0.7 μm (Ra) for the cylindrical specimens. The specimens were heat treated as described by Tobi et al. [11]. Fretting tests were conducted with four different specimen pair contact configurations; the CoF configurations were set up as shown in Fig. 2**a**, where the bottom specimen has a flat contact surface, and the top specimen has a cylindrical contact surface of radius R. For the C×C contact configuration, Fig. 2**b**, two cylindrical specimens of the same radius, R, are set up with the specimen axes perpendicular to each other. For each configuration, cylindrical specimens with $R = 6$ mm and $R = 160$ mm were utilised.

2.2. *Test procedures*

2.2.1. *Test apparatus*

A schematic diagram of the fretting test rig is shown in Fig. 3. Prior to testing, the specimens were degreased using detergent, cleaned with industrial methylated spirit (IMS), and air dried. A specimen was mounted on the lower specimen mounting block (LSMB) of the fretting test rig, and the other specimen on the upper specimen mounting block (USMB). All tests were conducted in air under ambient laboratory conditions, utilising a set of test conditions that allowed direct comparison with a body of previous work that has been conducted at the University of Nottingham using the same test rig. Specifically, a constant normal load P was applied on top of the USMB using a lever arm and a dead weight. The LSMB was held stationary whilst an oscillating motion with a far-field displacement amplitude Δ^* was applied to the USMB using an electromagnetic vibrator at a fixed frequency f. The duration of all tests conducted in this work was 1 million cycles since previous work had indicated that this was sufficient for the development of steady state wear conditions [8].

Table 2
Mechanical properties of BS S132 [12].

σ_y/MPa	σ_{UTS}/MPa	HV30	E/GPa	ν
1247	1697	485 ± 10	206.8	0.28

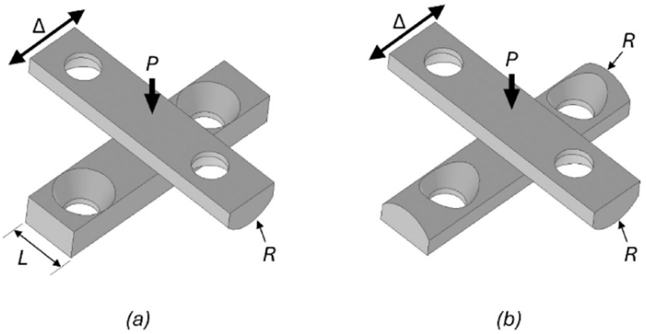

Fig. 2. Specimen pair setup in the (a) cylinder-on-flat (CoF) configuration, and (b) crossed-cylinder (C×C) configuration. In both configurations, R is the cylinder radius, P is the applied load, Δ is the applied displacement and L is the contact line length in the CoF configuration.

A control and data acquisition system programmed in LabVIEW, was used to record test data. A CS08 Micro-Epsilon capacitance displacement sensor was used to monitor the relative displacement (Δ) between the USMB and LSMB. A Kistler 9132BA Slimline piezoelectric load cell was used to monitor the tractional force (Q). The displacement sensor exhibited an accuracy of ± 0.2 % of the 700 μm full-scale output (FSO), while the load cell exhibited an accuracy of ± 2 % of the 5 kN FSO. The displacement (Δ) and tractional force (Q) can then be plotted in the form of fretting loops of the type shown schematically in Fig. 4 [10]. Post-processing of these data allows the dissipated energy in each fretting cycle (E_i) to be calculated [14], which is the area enclosed in a fretting loop. The total dissipated energy in a test (E) is the sum of the dissipated energy for each loop across all fretting cycles. Also, the slip amplitude (δ^*) (distinct from the applied displacement amplitude, Δ^*) can be calculated for each loop, this being the displacement at zero

Table 1
Chemical composition of BS S132 steel (wt%) [11].

C	Si	Mn	P	Cr	Mo	Ni	V	Fe
0.35–0.43	0.1–0.35	0.4–0.7	< 0.007	3.0–3.5	0.8–1.1	< 0.3	0.15–0.25	Balance

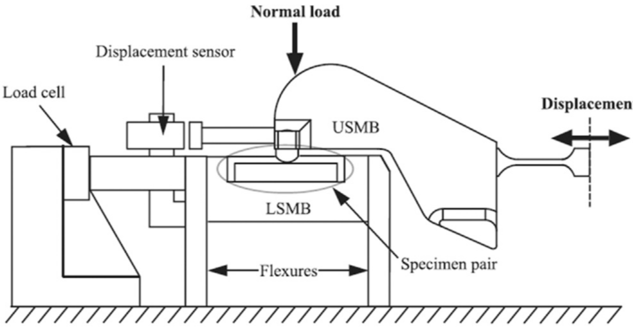

Fig. 3. Schematic diagram of the fretting rig [13].

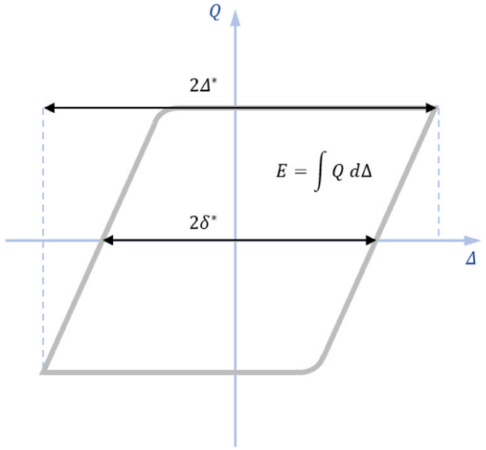

Fig. 4. An idealised fretting loop in the gross-slip regime.

tractional load (Q).

2.2.2. *Characterisation of wear and its evolution*

After testing, the worn specimens were firstly ultrasonically cleaned in an IMS bath to remove loose debris. Optical profilometry using an Alicona G5 was performed to enable the evaluation of worn volumes and wear depths of the individual samples, with the total wear volume (V) simply being the sum of the wear volumes of the two individual samples. Repeated tests have indicated a standard error of the mean below 6 % (in the range of similar tests carried out using the same methods and test rig [8]).

Once the total worn volume (V) and energy dissipated (E) had been calculated for each test, the size-dependent specific wear rate (k_{sd}) could be evaluated via Eq. (4) or Eq. (5) (as appropriate to the contact configuration).

In non-conforming contacts, the contact size changes as wear proceeds (both in terms of width and depth) and along with this, the contact pressure changes too. For both the CoF and the C×C contact configurations, the initial contact sizes and pressures were calculated using the appropriate standard elastic (Hertzian) contact equations. Having demonstrated that the total wear volumes take the form of the appropriate geometrical volume of intersection of one body with the other (see Fig. 1), then the development of the scar sizes (specifically, scar width ($2a$ or $2b$) and scar depth (h)) and the mean contact pressure across the scar (p_m) as the wear test proceeds can be described by the following equations [6].

For CoF contacts, the following equations apply:

$$b = \left(\frac{2\,E\,k_{sd}\,R}{L}\right)^{1/4} \tag{6}$$

$$h = \frac{b^2}{2\,R} \tag{7}$$

and

$$p_m = \frac{P}{2\,b\,L} \tag{8}$$

For C×C contacts, the following equations apply:

$$a = \left(\frac{5\,k_{sd}\,R\,E}{\pi}\right)^{1/5} \tag{9}$$

$$h = \frac{a^2}{2\,R} \tag{10}$$

and

$$p_m = \frac{P}{\pi\,a^2} \tag{11}$$

When the elastic contact size was greater than the predicted contact size as a result of wear (calculated using either Eq. (6) or Eq. (9) as appropriate), then the elastic equations were used. Once the contact size associated with wear was greater than that the initial elastic contact size, then Eqs. (6)–(11) were employed as appropriate.

The morphology of worn surfaces was characterised using a JSM-IT200 scanning electron microscope (SEM) utilising backscattered electron (BSE) and energy-dispersive X-ray (EDX) imaging techniques. SEM was performed both on as-worn surfaces and upon cross-sections through those surfaces. In such cases, the top specimen was sectioned using a high-speed cutting wheel so that the cutting plane was parallel to the direction of fretting motion. The section was mounted in conductive phenolic resin, ground with increasingly fine silicon carbide papers, with a final polish with 1 μm diamond paste before etching with 5 % nital.

2.3. *Test programme*

Both the cylinder-on-flat (CoF) and crossed-cylinder (C×C) contact configurations were examined. The CoF configuration featured top specimens with radii of $R = 6$ mm or $R = 160$ mm, creating two distinct setups: R6-on-flat and R160-on-flat; these are referred to as CoF R6 and CoF R160, respectively. The C×C configurations have specimen pairs of radii $R = 6$ mm or $R = 160$ mm to form configurations of either R6-on-R6 or R160-on-R160; these are referred to as C×C R6 and C×C R160, respectively. All the fretting tests were conducted under the conditions outlined in Table 3, with these values being selected to align with previous work which had been conducted at the University of Nottingham. The radii and two contact configurations were chosen to provide a wide range of initial contact pressures and rate of development of contact characteristics as wear proceeds. The evolution of wear in fretting conditions is known to be sensitive to fretting frequency and amplitude, and thus these were not varied within this test programme so that a clear understanding of the role of contact configuration itself could be developed.

Table 3
Conditions of the fretting tests conducted.

Cylinder radii R/mm	**Normal load** P/N	**Displacement amplitude** Δ^*/μm	**Frequency** f/Hz	**Test duration** N/cycles
6, 160	450	50	20	10^6

3. Results

3.1. Justification of spherical cap geometry for C×C contact configuration

As mentioned earlier, it is proposed that the total wear volume (V) across the two specimens will either be that of a prismatic minor segment of the circle (for a CoF contact configuration) or of a spherical cap (for a C×C contact configuration) (see Fig. 1) [9]. If these ideal geometries of the wear volumes are assumed, then V can be related to the wear scar dimensions as indicated in Eq. (12) or Eq. (13) [6].

For the CoF contact configuration:

$$V = \frac{2\,b^3\,L}{3\,R} \tag{12}$$

For the C×C contact configuration:

$$V = \frac{\pi\,a^4}{4\,R} \tag{13}$$

As such, one method of assessing the validity of the proposal is to examine whether experimentally measured wear volumes and contact widths accord with the relevant equation. Thus in Fig. 5, the product of the measured wear volumes and the relevant cylinder radius are plotted against the measured wear scar widths (either $2a$ or $2b$) for tests conducted with both the CoF and C×C contact configurations, with lines which represent the proposed geometrical relationships indicated by Eq. (12) and Eq. (13) for the CoF and C×C contact configurations, respectively. It should be noted that the data in Fig. 5 contain additional experimental results from tests outside of the tests reported in this paper. The additional tests were conducted with the same specimen configurations and materials, but with different fretting conditions. It can be seen that the measured data accord well with the idealised geometrical relationship for both contact configurations considered, which justifies the use of Eq. (12) or Eq. (13) in the derivation of Eq. (4) or Eq. (5), respectively.

3.2. The role of contact configuration in evolution of wear

The experimental results from the tests in the four contact configurations are presented in Table 4 along with values of the size-dependent specific wear rate (k_{sd}) as calculated using Eq. (4) or Eq. (5), as appropriate.

During fretting tests, it is the displacement amplitude (Δ^*), not the actual slip amplitude (δ^*), that is controlled. The slip amplitudes, averaged over all test cycles for each case (see Table 4), show consistent values relative to the applied displacement amplitude ($\Delta^* = 50$ μm). The lowest and highest δ^* values are 81 % and 88 % of Δ^*, for the CoF R6 and CoF R160, respectively, with this difference indicating that different contact configurations exhibit different tractional contact stiffness [15]. Similarly, the total dissipated energy (E) across all four contact configurations are very similar (Table 4), all being within ± 3 kJ of the average E (57.3 kJ), with a maximum uncertainty of ± 1.3 kJ.

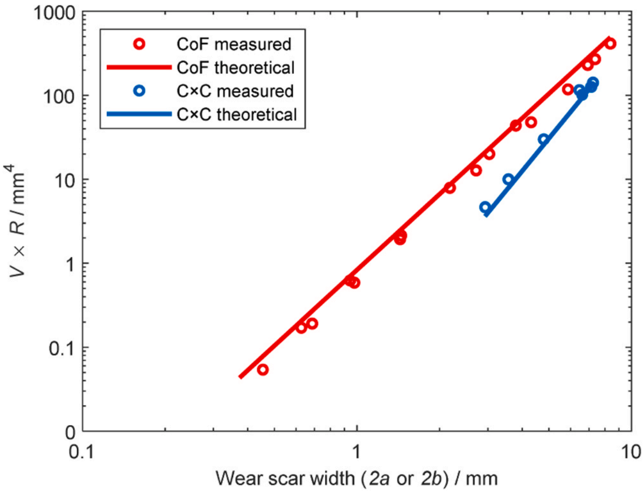

Fig. 5. Plot of the wear scar width against the product of net wear volume and cylinder radius for fretting tests conducted with R6 and R160 specimens in both CoF and C×C contact configurations. Measured data are shown against the idealised geometrical relationships.

Table 4
Tabulated experimental results for the CoF and C×C contact configurations examined.

Parameter	Unit	CoF		C×C	
		R6	R160	R6	R160
Slip amplitude (δ^*)	μm	40	44	42	43
Dissipated energy (E)	kJ	55.0	56.6	57.8	59.9
Worn volume (V)	mm^3	2.08	0.72	1.66	0.80
Size-dependent specific wear rate (k_{sd})	mm^4 MJ^{-1}	35.0	24.5	43.5	38.5

Despite the similarity in the dissipated energy in the four tests, V vary by a factor of three (Table 4), with the two R6 configurations exhibiting larger wear volumes than their R160 counterparts. However, the values of the size-dependent specific wear rate (k_{sd}) vary by only a factor of 1.8.

SEM-BSE micrographs in plan and cross-sectional views are presented in Fig. 6**a** and **b**, respectively. In the micrographs, oxides appear as dark grey in contrast compared to the lighter metallic material, due to their lower average atomic number. In all cases, the worn scars were covered with oxide layers to varying degrees (Fig. 6**a**). The CoF R6, CoF R160, and C×C R6 configurations all show relatively coherent oxide-debris coverage across the wear scar; in contrast, there are large areas on the surface of the samples from the C×C R160 tests where debris bed removal has taken place leaving the metallic surface exposed. The cross-sectional etched micrographs in Fig. 6**b** show the thickness of the debris bed formed and the degree of subsurface damage due to plastic deformation in each case. The specimens from the CoF R6 and C×C R6 tests exhibit a coherent oxide-debris bed and very little subsurface damage. The specimen from the CoF R160 test exhibits a layered debris-bed; the lower layer contains particles of higher contrast material in BSE imaging, indicating that there are metallic particles in the debris bed. In addition, some subsurface plasticity can be observed, with this having a depth ranging from approximately 2 μm to 10 μm. The specimen from the C×C R160 test shows no evidence of a debris bed being present; in addition, severe subsurface damage of the order of 10 μm in depth can be observed across the whole the section presented. However, a wider view of the same (C×C R160) surface shows significant variation (Fig. 7) with significant regions that do not exhibit subsurface plastic deformation. In addition, whilst no coherent debris bed has formed, relatively small patches of partially developed debris beds have formed (Fig. 7). Further analysis of these regions via EDX maps as presented in Fig. 8 show the oxygen and iron content in the regions with partially developed debris beds and also in the regions exhibiting subsurface plasticity. The characteristic fragmentation pattern observed in the partially developed debris beds (Fig. 8**a**) has previously been observed in other work, such as that by Kirk et al. [10] and by Baydoun [16], in SEM BSE analyses of their alloy steel specimens. It is clear that this cracked debris layer is distinct from the metallic material below it (Fig. 8**a**) and is oxygen-rich (i.e. it is an oxide-based debris); in contrast, the heavily plastically deformed subsurface region has a very low oxygen content (Fig. 8**b**), indicating that this is simply a product of metal-metal contact (shear and potentially metal transfer between the first bodies) in the fretting process.

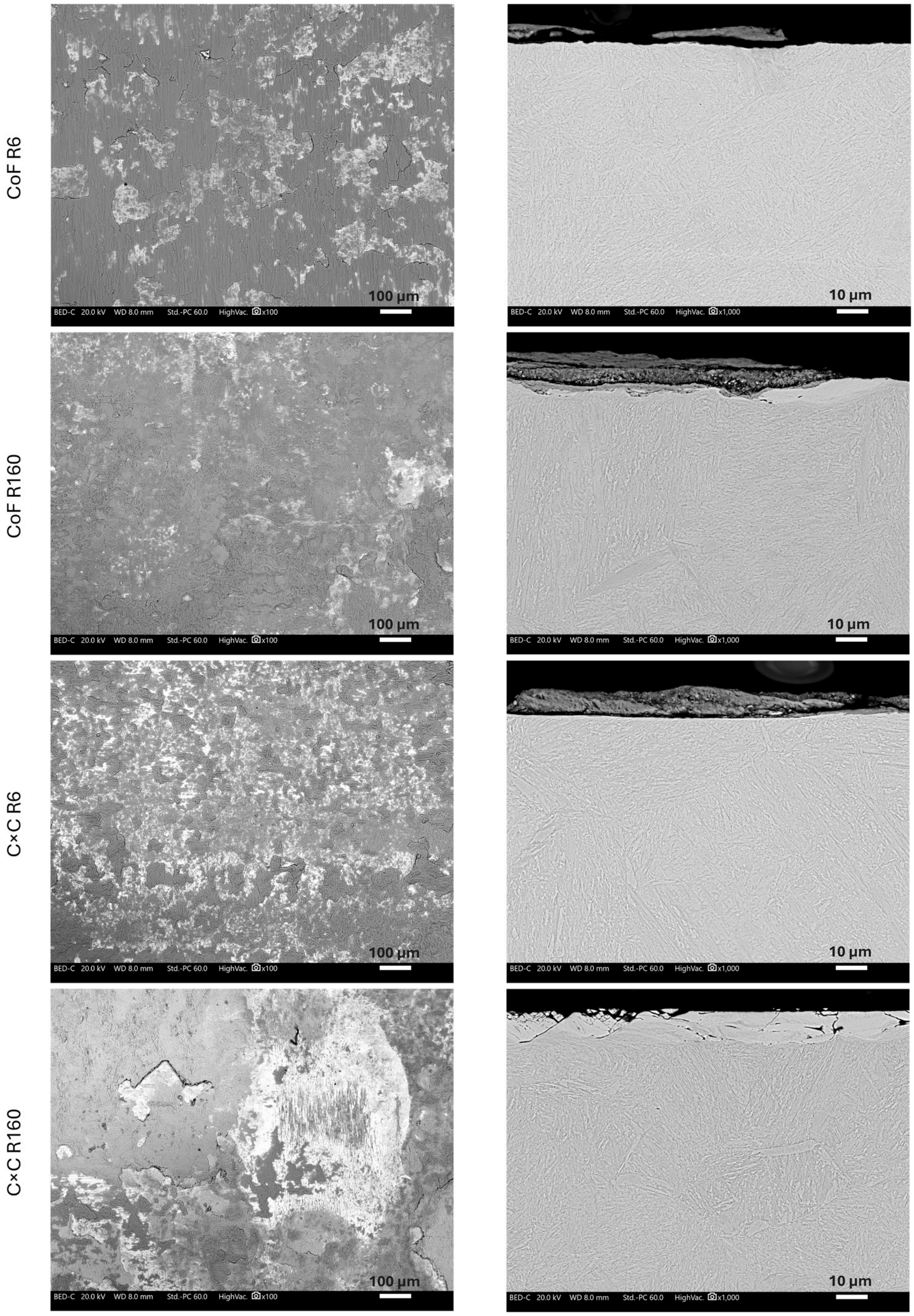

(a) Plan view (b) Cross-section

Fig. 6. Micrographs of specimens following testing with different contact configurations as indicated: (a) plan view SEM-BSE of the middle of the worn surfaces, and (b) SEM-BSE images of etched cross-sections the worn surfaces.

4. Discussion

4.1. *Validity of the model assumptions for the size-dependent specific wear rate for the two contact configurations*

In this work, the size-dependent specific wear rate (k_{sd}) has been calculated for the four cases considered with these values as presented in Table 4. The similarity of the values of k_{sd} from these tests provide further support for the validity of the model upon which the concept of k_{sd} is based. However, there are differences in the values which should be noted and discussed.

For specimens of a given radius (R), k_{sd} is larger for the C×C contact configuration than it is for the CoF contact configuration. It is proposed that this difference is due to the fact that in the derivation of the original model, transport of species (either oxygen or debris) was assumed to take place only in the direction of fretting, and “side-leakage” (transport in and out of the contact patch in other directions) was specifically neglected [1]. It is suggested here that the significance of side-leakage increases as the ratio of the dimension of the contact patch perpendicular to the fretting motion to the dimension of the contact patch parallel to the fretting motion falls. In the C×C contact configuration, this ratio is always unity, whereas for the CoF contact configuration, this ratio is

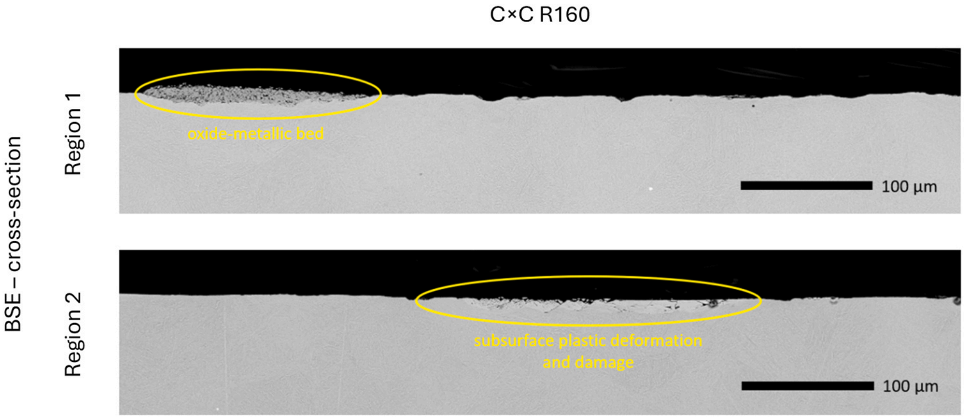

Fig. 7. Cross-sectional SEM-BSE micrographs showing two regions exhibiting a patch with an oxide-metallic bed (region 1) and subsurface plastic deformation and damage (region 2) in the C×C R160 case.

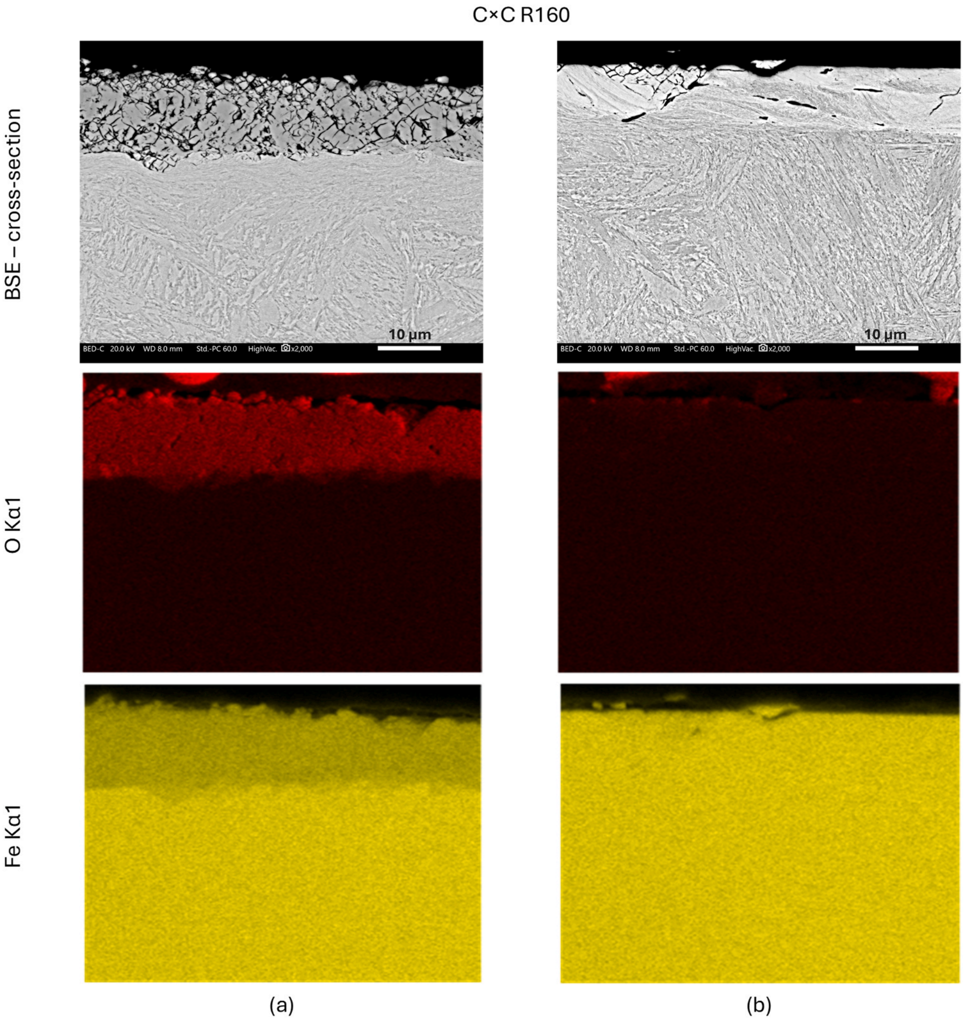

Fig. 8. C×C R160 cross-sectional SEM-BSE micrographs and EDX maps for regions associated with the regions in Fig. 7: (a) region with a distinct oxygen-rich debris layer; (b) region showing severe subsurface plasticity.

very large initially ($L = 10$ mm in the work presented here) and falls as the tests proceed. It is suggested that the larger values of k_{sd} for the C×C contact configuration are associated with the greater significance of side-leakage in this case. It is also noted that in each contact configuration, k_{sd} is larger for the smaller values of contact radius, R. The fact that this is observed for the tests with the C×C contact configuration indicates that this is not associated with differences in side-leakage, since the ratio of the dimension of the contact patch perpendicular to the fretting motion to the dimension of the contact patch parallel to the fretting motion does not change with R in this contact configuration. Whilst side-leakage was neglected in the original model for both oxygen flow into the contact and debris flow out of the contact, it is suggested here that the significance of side-leakage is likely to be different for these two transport processes; specifically, it is argued that enhancement of the rate of transport in the direction of the fretting motion will be more significant for debris egress than it is for oxygen ingress, as illustrated schematically in Fig. 9. Accordingly, it is expected that side-leakage will have a more significant impact on the value of k_{sd} for situations where oxygen ingress is the RDP as opposed to those where debris egress is the RDP. Where side leakage is significant, a higher value of k_{sd} is expected and it is therefore argued that the larger contact radii (in both contact configurations) lead towards oxygen transport into the contact being the RDP.

The data presented here therefore provide support for the model, but also indicate that further refinements to the model to account for side-leakage are required, with these addressing the suggestion that the significance of side-leakage is likely to be different for the two key transport processes (namely oxygen and debris transport).

4.2. Evolution of contact conditions during wear

Whilst the applied conditions of the fretting tests in the four contact configurations were the same, the conditions in the contact were very different, both initially and in their evolution. The Hertzian contact widths and mean contact pressures in each case are presented in Table 5 where it can be seen that the over the four tests the Hertzian contact width varies by a factor of more than 14 whilst Hertzian contact pressure varies by a factor of more than 26.

The model for the development of wear allows the development of the wear scar dimensions (and therefore contact pressure) throughout the wear test to be predicted via Eqs. (6)–(11). Using the appropriate equations and the values of E and k_{sd} as presented in Table 4, the predicted evolution of contact width (b in the case of the CoF contact configuration and a in the case of the C × C contact configuration), contact depth (h) and average contact pressure (p_m) are presented in Fig. 10**a**–**c**, respectively.

4.2.1. Development of contact width during wear

It can be seen from Fig. 10**a** that as a result of wear, the contact width increases, with this exceeding the size of the Hertzian contact width very early in the tests under the conditions employed in this work; once E has exceeded 0.03 kJ (in this case ~ 0.5 ‰ of the total test duration), all the contact sizes (and therefore contact pressures) are controlled not by the initial elastic conditions, but instead by the amount of wear that has taken place. Although the elastic contact widths varied by a factor of 14 over these four tests, it can be seen that by the end of the tests, the contact widths vary by a factor of less than 3.

The development of contact size with energy dissipated is different for the two contact configurations; in the case of CoF contact configuration, $b \propto E^{1/4}$ (Eq. (6)), whereas for the C×C contact configuration, $a \propto E^{1/5}$ (Eq. (9)), the differences in exponent resulting in the difference in the gradients observed on the log-log presentation of the data in Fig. 10**a**. The rate of growth of contact size with energy dissipated is more rapid for the CoF contact configuration than for the C×C contact configuration; for example, although the Hertzian contact width was relatively similar in the CoF R160 and the C×C R6 cases here (see Table 5 and Fig. 10**a**), by the end of the test, the contact width in the CoF case was ~ 38 % higher than in the C×C case. However, it is clear that once the contact widths are controlled by wear, then for a particular contact configuration, the ratio of the contact width is simply proportional to the ratio of the contact radii raised to the power of either 1/4 or 1/5 (as appropriate to the contact configuration) at any energy dissipated.

Table 5
Initial Hertzian contact size and contact pressures in the four contact configurations considered.

Parameter	Unit	CoF		C × C	
		R6	R160	R6	R160
Hertzian contact size (a or b as appropriate)	μm	55	286	262	784
Hertzian mean contact pressure (p_m)	MPa	406	79	2082	233

4.2.2. Development of contact depth during wear

Before any discussion relating to the evolution of wear scar depth during tests, it should be noted that the wear scar depth (h) is the sum of the individual scar depths on the two specimens, irrespective of how the wear is apportioned between the two specimens. In the case where the materials making up the two specimens in the couple are the same (as in this work), it is not unreasonable to assume that the wear depth on each specimen is simply $h/2$.

As can be seen from Eq. (7) and Eq. (10), the wear scar depth (h) is proportional to the square of the appropriate contact width for both the CoF and C×C contact configurations. In the case of CoF contact configuration, it can be seen that this will result in $h \propto E^{1/2}$ (following from Eq. (6)), whereas for the C×C contact configuration, this will result in $h \propto E^{2/5}$ (following from Eq. (9)), the differences in exponent resulting in the difference in the gradients observed on the log-log presentation of the data in Fig. 10**b**. As such, as was the case for the contact width, the rate of growth of wear depth with energy dissipated is more rapid for the CoF contact configuration than for the C×C contact configuration as can be seen from the examples presented in Fig. 10**b**. As previously, it is clear that for a particular contact configuration the ratio of the worn contact depths is simply proportional to the ratio of the contact radii raised to the power of either 1/2 or 2/5 (as appropriate to the contact configuration) at any energy dissipated.

In the initial stages of wear, the development of wear will be influ-

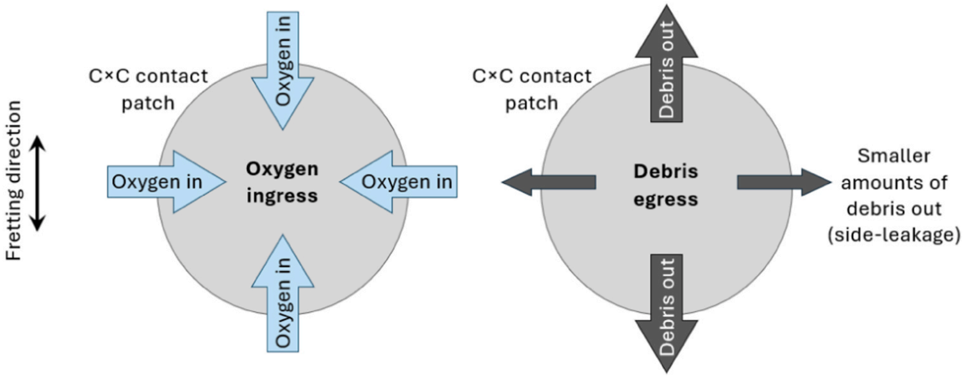

Fig. 9. An illustration of proposed influence of fretting direction on transport rates of species (oxygen and debris) in and out of a fretting contact for a C×C contact configuration.

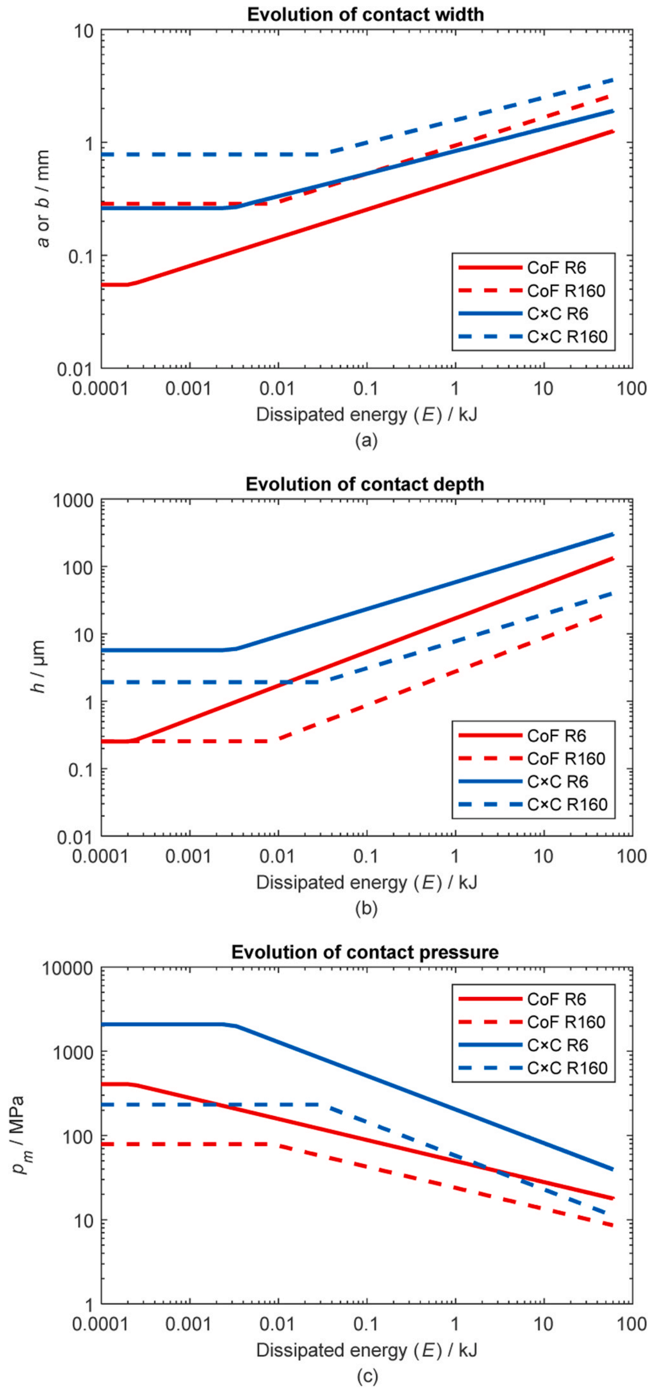

Evolution of contact width

Evolution of contact depth

Evolution of contact pressure

Fig. 10. Predicted development of contact conditions throughout the tests conducted with the four contact configurations as indicated: (a) contact size (a or b); (b) maximum wear depth (h); (c) average contact pressure in the wear scar (p_m).

enced by (amongst other things) the initial (as-prepared) surface roughness of the samples. In terms of the development of wear in fretting, it is expected that the surface roughness will exert a significant influence if the depth of the wear scar on an individual sample ($h/2$) is less than the initial surface roughness (and may exert and influence even when the wear is deeper). In this work, all samples were produced with an Ra of < 0.7 μm, and this value will be employed for further discussion. For the four cases examined, the energy dissipated when h has reached 1.4 μm (i.e. the wear depth of each specimen has reached the value of its surface roughness of 0.7 μm) is shown in Table 6. For all contact configurations, the energy required to reach that critical wear depth is very small (< 0.5 %) compared to the total energy dissipated in the tests (between 55 kJ and 60 kJ). In addition, the wear depth at the end of the tests is also tabulated (Table 6); it is seen that for the contact length utilised in these CoF contact configurations, the wear depth is generally lower in the CoF contact configurations than in the C×C contact configurations, and is smaller for the larger radius of the contacting elements (R) within each configuration.

Table 6

Predictions of energy dissipated when the wear depth first exceeds the surface roughness (with a value of Ra of 0.7 μm) along with the predicted depth of wear at the end of the test for the four contact configurations considered.

Parameter	**Unit**	**CoF**		C × C	
		R6	**R160**	**R6**	**R160**
Energy dissipated when $h = 1.4$ μm	J	7	256	0	0
Depth of wear, (h) at end of test	μm	132	21	302	40

The equations for the total wear depth are as follows [6]. For the CoF contact configuration:

$$h = \left(\frac{E\,k_{sd}}{2\,L\,R}\right)^{1/2} \tag{14}$$

and for the C×C contact configuration:

$$h = \left(\frac{5\,k_{sd}\,E}{\sqrt{32}\;\pi\,R^{3/2}}\right)^{2/5} \tag{15}$$

As can be seen, the wear depths depend upon a number of parameters, including the contact geometrical parameters, (R and L), the energy dissipated in the test (E) and the size-dependent specific wear rate itself (k_{sd}). Tests need to be designed to ensure that the depth of wear on each specimen is significantly greater than the surface roughness of that specimen to ensure that surface roughness effects do not significantly influence the wear behaviour observed.

4.2.3. *Development of contact pressure during wear*

It can be seen from Fig. 10**c** that as a result of wear, as the contact width increases, the contact pressure decreases, with this falling below the Hertzian contact pressure very early in the tests under the conditions employed here; once E has exceeded 0.03 kJ (in this case ~ 0.5 ‰ of the total test duration), all the contact pressures are controlled not by the elastic conditions, but instead by the amount of wear that has taken place. Although the initial Hertzian contact pressures varied by a factor of 26 over these four tests, it can be seen that by the end of the tests, the contact pressures vary by a factor of less than 5. Even after only 10 % of the total energy of these tests has been dissipated (~ 6 kJ), the ratio of the highest to lowest contact pressure has reduced to only 6.5.

In the case of CoF contact configuration, it can be seen that $p_m \propto E^{-1/4}$ (by eliminating b between Eq. (8) and Eq. (6)) whereas for the C×C contact configuration, $p_m \propto E^{-2/5}$ (by eliminating a between Eq. (11) and Eq. (9)), the differences in exponent resulting in the difference in the gradients observed on the log-log presentation of the data in Fig. 10**c**. As such, the rate of decrease of the contact pressure with energy dissipated is more rapid for the C×C contact configuration than for the CoF contact configuration. As previously, it is clear that once the contact widths are controlled by wear, then for a particular contact configuration, the ratio of the contact width is simply proportional to the ratio of the contact radii raised to the power of either $-1/4$ or $-2/5$ (as appropriate to the contact configuration) at any energy dissipated.

A key recommendation here is that tests with conforming contact configurations should be run for extended periods since this results in a reduction in the rate of change of contact pressure with energy dissipated.

4.2.4. Summary of evolution of contact conditions during testing

The preceding discussion has focussed on the way that the different parameters vary during fretting tests as a function of energy dissipated. It has been seen that for all the parameters considered (wear volume (V), wear scar width (b or a), wear scar depth (h) and mean contact pressure in the scar (p_m)), the magnitude of the rate of change of the parameter with energy dissipated decreases as E increases, but with different dependencies upon E. These are more clearly observed in the derivatives themselves, and these are therefore presented in the following equations.

For the CoF contact configuration:

$$\frac{db}{dE} = \left(\frac{k_{sd}\,R}{128\,E^3\,L}\right)^{1/4} \tag{16}$$

$$\frac{dh}{dE} = \left(\frac{k_{sd}}{8\,L\,E\,R}\right)^{1/2} \tag{17}$$

$$\frac{dp_m}{dE} = -\frac{P}{8\left(2\,L^3\,E^5\,k_{sd}\,R\right)^{1/4}} \tag{18}$$

For the C×C contact configuration:

$$\frac{da}{dE} = \left(\frac{k_{sd}R}{625\,\pi\,E^4}\right)^{1/5} \tag{19}$$

$$\frac{dh}{dE} = \left(\frac{k_{sd}}{\sqrt{125}\;\pi\,E^{3/2}\,R^{3/2}}\right)^{2/5} \tag{20}$$

$$\frac{dp_m}{dE} = -\frac{2\,P}{\left(5^{7/2}\,\pi^{3/2}\,k_{sd}\,R\,E^{7/2}\right)^{2/5}} \tag{21}$$

From these it can be seen that for both the CoF and C×C contact configurations, the rate of change of all three parameters (i.e. $\frac{d}{dE}$) falls as E increases (i.e. as the test progresses). However, it can be seen that for both the CoF and C×C contact configurations, the rate of change of wear scar depth (h) and mean contact pressure in the scar (p_m) as the test proceeds (i.e. $\frac{d}{dE}$) decreases as R is increased, but that the rate of change of wear scar width (b or a) as the test proceeds (i.e. $\frac{d}{dE}$) increases as R is increased.

To illustrate these changes more clearly, the changes in the four parameters over a test of an arbitrary duration (represented by the energy dissipated E) for both contact configurations are illustrated in Fig. 11. In each case, the parameters at the end of the test are indicated (wear volume (V), wear scar width (b or a), wear scar depth (h) and mean contact pressure in the scar (p_m)), along with the values of those same parameters (as a ratio) after just 10 % of the test duration. After 10 % of the test duration, the smallest degree of change is associated with the wear scar width (b or a) with this already being at 0.562 or 0.631 of its final value (for the CoF and C×C contact configurations, respectively). Using the C×C contact configuration as an example, the contact size will only change from 0.631 a to a over the final 90 % of a test.

The rates of increase in wear scar depth (h) are more significant than those for wear scar width (b or a) for both contact configurations. In addition, it can be seen that the rate of decrease in mean contact pressure in the scar (p_m) is much larger for the C×C contact configuration than it is for the CoF contact configuration, as expected.

4.3. Debris beds and subsurface damage in the different contact configurations

Microstructural work shows that the nature of debris bed formation and sub-surface damage is also dependent upon the details of the contact configuration across the four cases examined. Table 7 provides a summary of the observations for the four cases examined.

In both of the R6 contact configurations (CoF R6 and C×C R6), there is no evidence of plastic deformation in the microstructure of the first bodies below the oxide debris bed. This implies that in these cases, the material removal from the first bodies in fretting takes place by abrasion of the first body by debris within the debris bed.

In addition to this observation, it is clear that the R160 specimens (in both the CoF and C×C configurations) result in more sub-surface damage in the microstructure (plastic deformation) than is observed with the R6 specimens which implies that there has been significant metal-metal contact during the fretting process and that therefore that an oxide debris bed has not effectively separated the surfaces. It might be expected that such differences could be associated with contact pressure (where high contact pressures might be expected to result in severe subsurface plastic deformation) or with contact size (where differences may be due to changes in the rates of oxygen transport to form oxide and debris transport out of the contact to allow wear to proceed). Fig. 10**c** shows that throughout the tests, the mean pressure in the contact is significantly higher in the C×C R6 contact configuration than it is in any

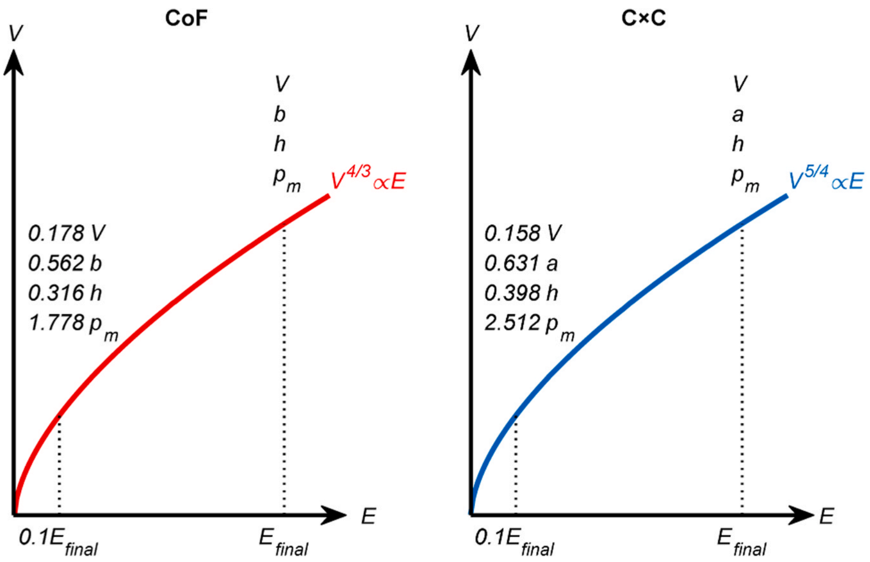

Fig. 11. Schematic diagrams of development of V with E for the CoF and C×C contact configurations, respectively, showing the ratios of the four parameters associated with the wearing contact at 10 % into the test (0.1E_{final}) to those at the end of the test (E_{final}).

Table 7
A summary of observations from the CoF and C×C tests SEM-BSE plan view and cross-sectional micrographs.

	CoF R6	CoF R160	C×C R6	C×C R160
Scar surface coverage	Mainly oxide	Mainly oxide	Mainly oxide	Oxide & metal
Subsurface damage	Low/None	Limited	Low/None	Severe

of the other cases; in light of this, we argue that the subsurface damage in the fretting tests conducted here does not depend upon the mean pressure in the contact. However, Fig. 10**a** shows that throughout the tests, the contact width is significantly higher in the C×C R160 contact configuration than it is in any of the other cases (and that the second largest by the end of the tests is in the CoF R160 contact configuration). We argue that the correlation between contact width (and not the other features of the contact, such as mean pressure) at the end of the test and subsurface plasticity is a causal relation, with this being associated with relative changes in the rates of the two transport mechanisms.

In the case of the C×C R160 contact configuration, further characterisation demonstrated that oxide debris was forming in certain isolated areas across the surface (Fig. 7) with this oxide being brittle and exhibiting shear fracture. It is notable too that even in the region where this oxide was forming, there was evidence of sub-surface plasticity in the first bodies (Fig. 8**a**).

5. Conclusions

In this work, the concept of the derivation of a size-dependent specific wear rate from fretting tests with non-conforming contact configurations has been explored. Fretting tests were conducted with CoF and C×C contact configurations with both R6 and R160 cylindrical specimens; it was shown that despite the very different initial contact conditions (contact size and contact pressure), wear reduced the differences between these very quickly.

The model which underpins the concept of a size-dependent specific wear rate depends upon a hypothesis that the combined wear volume of the two bodies in the contact can be described by the geometrical volume of intersection of one body with the other. This has previously been shown to be the case for CoF contact configurations, and in this work, it has been demonstrated that this is also a valid hypothesis for C×C contact configurations, thus adding to the robustness of the case for the use of equations relating to the evolution of the wear volume, contact size, contact depth and mean contact pressure in the contact for tests conducted with C×C contact configurations.

The size-dependent specific wear rates evaluated from the four test configurations were similar (between 24.5 and 43.5 $\text{mm}^4\ \text{MJ}^{-1}$). The similarity of these values in spite of the very different evolutions of contact conditions in the four configurations examined provides further support for the model which underpins their evaluation, and suggests that by use of the size-dependent specific wear rate, tests from the literature which have been conducted with different contact configurations can be compared with confidence.

Quantitative predictions of the evolution of the wear scar size, wear scar depth and contact pressure in the wear scar have been produced for the four contact configurations examined. It has been shown that the wear scar size (and therefore the mean pressure across the contact) and wear scar depth develop very rapidly in the early stages of a test, but that in the last 90 % of a test will vary relatively slowly compared with the rate at which the wear volume develops.

Examination of worn specimens revealed differences in the modes of damage in the specimens from the four test configurations. In particular, sub-surface plasticity was seen in the metallic R160 specimens (much more severe in the C×C contact configuration than in the CoF contact configuration), but was not seen in either of the test configurations with the R6 specimens; in these cases, a debris bed on the surface prevented metal-metal contact between the two first bodies and thus no gross subsurface deformation was observed. It was shown therefore that the presence or absence of sub-surface plasticity and damage in the first bodies was associated with the size of the wearing contact and not with the contact pressure; under a given set of conditions, smaller contact sizes were seen to favour formation of debris beds which limit metal-metal contact and vice versa.

CRediT authorship contribution statement

Philip H Shipway: Writing – review & editing, Writing – original draft, Validation, Supervision, Methodology, Conceptualization. **Allan J Gichuki:** Writing – review & editing, Writing – original draft, Validation, Methodology, Investigation, Conceptualization. **Euan Coll:** Validation, Conceptualization. **Daniel Koti:** Validation, Conceptualization. **Chris J Bennett:** Writing – review & editing, Supervision, Funding acquisition, Conceptualization. **James P Rouse:** Writing – review & editing, Supervision, Methodology, Funding acquisition, Conceptualization.

Funding statement

A.J. Gichuki is a PhD student at the University of Nottingham and his studentship is funded by Rolls-Royce plc and the EPSRC (Grant ref. EP/W524402/1). A.J. Gichuki is also supported by the Whitworth Society through a Whitworth Senior Scholarship Award.

Declaration of Competing Interest

The authors declare no conflicts of interest relevant to the content of this work. Allan J. Gichuki is a PhD student at the University of Nottingham and his studentship is funded by Rolls-Royce plc and the EPSRC. Allan J. Gichuki is also supported by the Whitworth Society through a Whitworth Senior Scholarship award. None of these funding sources had involvement in the study design, data collection, analysis, or interpretation of the results of this work.

All authors confirm that the research was conducted with full academic independence and integrity. Any affiliations, financial contributions, or collaborative efforts have been clearly acknowledged within the manuscript

Acknowledgements

The authors thank the University of Nottingham for both financial and facility support. The authors would also like the thank the Nanoscale and Microscale Research Centre (nmRC) at the University of Nottingham for providing access to their instrumentation.

Declaration of competing interest

The authors declare that they have no known competing financial interests or personal relationships that could have appeared to influence the work reported in this paper.

Statement of Originality

We, the undersigned authors, hereby declare that the manuscript titled *" The evolution of contact conditions during fretting wear tests with cylinder-on-flat and crossed-cylinder specimen configurations"* is an original work conducted by us. This work has not been previously published and is not under consideration for publication elsewhere. All references and sources of information have been appropriately acknowledged, with proper citations provided for all external materials used.

This manuscript represents the collective contributions and independent research of all co-authors. Any collaborative efforts have been duly acknowledged within the manuscript. We further confirm that the research presented adheres to the ethical standards and guidelines of *Tribology International*.

By submitting this manuscript, we accept responsibility for its content and affirm that it accurately reflects our genuine findings and conclusions.

Data availability

Data will be made available on request.

References

[1] Shipway PH, Kirk AM, Bennett CJ, Zhu T. Understanding and modelling wear rates and mechanisms in fretting via the concept of rate-determining processes – contact oxygenation, debris formation and debris ejection. Wear 2021;486-487:204066. https://doi.org/10.1016/j.wear.2021.204066.

[2] Godet M. The third-body approach: a mechanical view of wear. Wear 1984;100(1):437–52. https://doi.org/10.1016/0043-1648(84)90025-5.

[3] Baydoun S, Fouvry S, Descartes S. Modeling contact size effect on fretting wear: a combined contact oxygenation - third body approach. Wear 2022;488–489:204168. https://doi.org/10.1016/j.wear.2021.204168.

[4] Baydoun S, Fouvry S, Descartes S, Arnaud P. Fretting wear rate evolution of a flat-on-flat low alloyed steel contact: a weighted friction energy formulation. Wear 2019;426-427:676–93. https://doi.org/10.1016/j.wear.2018.12.022.

[5] Fouvry S, Arnaud P, Mignot A, Neubauer P. Contact size, frequency and cyclic normal force effects on Ti–6Al–4V fretting wear processes: an approach combining friction power and contact oxygenation. Tribology Int 2017;113:460–73. https://doi.org/10.1016/j.triboint.2016.12.049.

[6] Shipway PH. The contact size dependence of wear rate in fretting: understanding and rationalising data from tests with flat-on-flat, cylinder-on-flat and sphere-on-flat contact configurations. Wear 2025:205783. https://doi.org/10.1016/j.wear.2025.205783.

[7] Shipway PH, Kirk AM, Bennett CJ, Zhu T. Corrigendum to 'Understanding and modelling wear rates and mechanisms in fretting via the concept of rate-determining processes – contact oxygenation, debris formation and debris ejection'. Wear 2022;488-489:204161. https://doi.org/10.1016/j.wear.2021.204161.

[8] Zhu T, Shipway PH, Sun W. The dependence of wear rate on wear scar size in fretting the role of debris (third body) expulsion from the contact. Wear 2019;440–441:203081. https://doi.org/10.1016/j.wear.2019.203081.

[9] Zhu T, Shipway PH. Contact size and debris ejection in fretting: the inappropriate use of Archard-type analysis of wear data and the development of alternative wear equations for commonly employed non-conforming specimen pair geometries. Wear 2021;474–475:203710. https://doi.org/10.1016/j.wear.2021.203710.

[10] Kirk AM, Sun W, Bennett CJ, Shipway PH. Interaction of displacement amplitude and frequency effects in fretting wear of a high strength steel: impact on debris bed formation and subsurface damage. Wear 2021;482–483:203981. https://doi.org/10.1016/j.wear.2021.203981.

[11] Mohd Tobi AL, Ding J, Pearson S, Leen SB, Shipway PH. The effect of gross sliding fretting wear on stress distributions in thin W-DLC coating systems. Tribol Int 2010;43(10):1917–32. https://doi.org/10.1016/j.triboint.2010.01.018.

[12] Leen SB, Richardson IJ, McColl IR, Williams EJ, Hyde TR. Macroscopic fretting variables in a splined coupling under combined torque and axial load. J Strain Anal Eng Des 2001;36(5):481–97. https://doi.org/10.1243/0309324011514647.

[13] Warmuth AR, Shipway PH, Sun W. Fretting wear mapping: the influence of contact geometry and frequency on debris formation and ejection for a steel-on-steel pair. Proc R Soc A Math Phys Eng Sci 2015;471(2178):20140291. https://doi.org/10.1098/rspa.2014.0291.

[14] SR Pearson. The effect of nitriding on the fretting wear of a high strength steel at ambient and elevated temperatures [Ph.D. Faculty of Engineering]. University of Nottingham; 2013.

[15] Kartal ME, Mulvihill DM, Nowell D, Hills DA. Measurements of pressure and area dependent tangential contact stiffness between rough surfaces using digital image correlation. Tribol Int 2011;44(10):1188–98. https://doi.org/10.1016/j.triboint.2011.05.025.

[16] Baydoun S. Investigation of fretting wear of a flat-on-flat 34NiCrMo16 interface: application and modelling of the contact oxygenation concept. Université de Lyon; 2020. ⟨https://theses.hal.science/tel-03167098⟩ [2020LYSEC030. [Online]].